Bayesian Inference and Global Sensitivity Analysis for Ambient Solar Wind Prediction

Opal Issan[1], Pete Riley[2], Enrico Camporeale[3,4], Boris Kramer[1]

[1]Department of Mechanical and Aerospace Engineering, University of California San Diego, La Jolla, CA, USA
[2]Predictive Science Inc., San Diego, CA, USA
[3]CIRES, University of Colorado, Boulder, CO, USA
[4]NOAA Space Weather Prediction Center, Boulder, CO, USA

Key Points:

- We quantify and reduce the parametric uncertainties of the PFSS, WSA, and HUX models on the ambient solar wind predictions near Earth.
- Global sensitivity analysis shows that the five most influential parameters are all numerical parameters in the WSA model.
- The posterior of the influential parameters changes greatly in time, motivating the investigation of the forecasting capability of WSA.

Corresponding author: Opal Issan, `oissan@ucsd.edu`

Abstract

The ambient solar wind plays a significant role in propagating interplanetary coronal mass ejections and is an important driver of space weather geomagnetic storms. A computationally efficient and widely used method to predict the ambient solar wind radial velocity near Earth involves coupling three models: Potential Field Source Surface, Wang-Sheeley-Arge (WSA), and Heliospheric Upwind eXtrapolation. However, the model chain has eleven uncertain parameters that are mainly non-physical due to empirical relations and simplified physics assumptions. We, therefore, propose a comprehensive uncertainty quantification (UQ) framework that is able to successfully quantify and reduce parametric uncertainties in the model chain. The UQ framework utilizes variance-based global sensitivity analysis followed by Bayesian inference via Markov chain Monte Carlo to learn the posterior densities of the most influential parameters. The sensitivity analysis results indicate that the five most influential parameters are all WSA parameters. Additionally, we show that the posterior densities of such influential parameters vary greatly from one Carrington rotation to the next. The influential parameters are trying to overcompensate for the missing physics in the model chain, highlighting the need to enhance the robustness of the model chain to the choice of WSA parameters. The ensemble predictions generated from the learned posterior densities significantly reduce the uncertainty in solar wind velocity predictions near Earth.

Plain Language Summary

Predicting the ambient solar wind is an important component of space weather forecasting. We use advanced statistical techniques to analyze the important parameters in a widely-used ambient solar wind model. The numerical results show that five specific parameters have the largest impact on solar wind model predictions near Earth and that these parameters can fluctuate considerably over time. The statistical results give us a deeper understanding of the limitations and potential improvements for enhancing the accuracy and reliability of ambient solar wind forecasts. Such an understanding is essential for mitigating the potential impacts of severe geomagnetic storms.

1 Introduction

The ambient (or background) solar wind is the long-lived large-scale plasma that emanates from the Sun and travels into interplanetary space, which excludes interplanetary coronal mass ejections and other transient events. It is crucial to accurately predict the ambient solar wind since interplanetary coronal mass ejections, the primary source of extreme space weather events, are modeled as perturbations to the ambient solar wind (Odstrcil & Pizzo, 1999). Additionally, corotating interaction regions between fast and slow ambient solar wind streams are drivers of moderate space weather events (Riley et al., 2012). In fact, corotating interaction regions have been found to contribute to 70% of geomagnetic activity at Earth during solar minimum and about 30% during solar maximum (Richardson et al., 2000). Thus, generating reliable predictions of the ambient solar wind is essential for improving space weather prediction capabilities and for accurately assessing the risk of space weather events.

State-of-the-art ambient solar wind models couple two regions: the corona and heliosphere. The coronal domain spans from the surface of the Sun ($1R_S$, i.e., one solar radius) up to the coronal outer boundary, which is typically set to a distance between $2.5R_S$ to $30R_S$ depending on the model that is used. The solution at the coronal outer boundary is extrapolated into the heliospheric domain up to Earth's orbit and beyond. High-fidelity simulations of the ambient solar wind are constructed via time-dependent magnetohydrodynamic (MHD) models, such as the Magnetohydrodynamics Algorithm outside a Sphere (Linker et al., 1999; Mikić et al., 2018; Riley et al., 2019) and the Space Weather Modeling Framework (Toth et al., 2005; van der Holst et al., 2014). Such MHD models simulate the ambient solar wind by relaxing the coronal and heliospheric simulations to a steady-state solution,

requiring high computational costs. In an effort to reduce simulation time (especially in operational settings), the space weather community commonly uses lower-fidelity models based on reduced physics and empirical relations. A well-established and widely-used chain of lower-fidelity models couples the Potential Field Source Surface (PFSS) (Altschuler & Newkirk, 1969; Schatten et al., 1969), Wang-Sheeley-Arge (WSA) (Arge et al., 2004), and Heliospheric Upwind eXtrapolation (HUX) (Riley & Lionello, 2011; Riley & Issan, 2021; Issan & Riley, 2022) models.

There has been a continuous effort in the space weather community to improve ambient solar wind models by comparing the model predictions to *in-situ* spacecraft observations (Reiss et al., 2022). Such *in-situ* observations can also be leveraged to reduce prediction uncertainties stemming from initial conditions, boundary conditions, fitting parameters, numerical errors, measurement noise, etc. There are two types of prediction uncertainty. *Aleatoric uncertainty* results from intrinsic randomness or variability associated with parameters, mesh resolution, initial conditions, etc; *epistemic uncertainty* results from a lack of complete knowledge of physics and model inadequacies. Here, we study aleatoric uncertainty, specifically parametric uncertainty, in the PFSS→WSA→HUX model chain. We rigorously examine the uncertainty and sensitivity of eleven mainly non-physical model parameters, such as the source surface height and WSA numerical parameters, and their impact on the solar wind radial velocity predictions near Earth. Quantifying and reducing the parametric uncertainties in the ambient solar wind models is critical for making informed decisions in operational settings.

As a core contribution of this work, we present a comprehensive uncertainty quantification (UQ) framework to advance the use of rigorous UQ techniques in space weather. The proposed UQ framework is described in the following steps. First, we perform variance-based global sensitivity analysis to identify which parameters influence the solar wind predictions near Earth the most. Subsequently, parameters that hardly contribute to the prediction variability are set to their fixed nominal values, which facilitates *a posteriori* parameter dimensionality reduction. Then, we apply Bayesian inference to uncover the posterior density of the influential parameters, which is the conditional probability of the influential parameters given observational data. Lastly, we sample from the learned posterior densities and generate an ensemble of the ambient solar wind predictions near Earth, which demonstrates that the UQ framework reduces the parametric uncertainty in the predicted solar wind velocity.

Sensitivity analysis quantifies the contribution of parametric uncertainty on the variability of a quantity of interest (QoI). Common methods can be classified into two groups: local and global. Local sensitivity analysis methods vary the parameters about a nominal value by computing local partial derivatives, whereas global sensitivity analysis methods account for variance effects in the entire parameter space (Saltelli et al., 2008). We use variance-based global sensitivity analysis by estimating Sobol' sensitivity indices (Sobol', 2001). A sensitivity analysis study by Jivani et al. (2022) estimated the Sobol' sensitivity indices associated with uncertain parameters in the MHD Alfvén Wave Solar atmosphere Model (van der Holst et al., 2014). A recent study by Reiss et al. (2020) used Morris screening (Morris, 1991), a hybrid local/global sensitivity analysis method, to identify the most influential parameters in the WSA model. The Morris screening method averages local derivative approximations to provide global sensitivity measures (Smith, 2013, §15.2). It is typically used when variance-based methods are prohibitively expensive since it can only rank the parameters based on their importance but, unlike variance-based methods, does not quantify the relative contributions of each parameter to the QoI variance. Our study differs from Reiss et al. (2020) since we consider parametric uncertainty stemming not only from WSA but also from PFSS and HUX. Additionally, our study differs from Reiss et al. (2020) since we compute full global sensitivity information.

Parameter estimation techniques are typically divided into two approaches: frequentist and Bayesian. The frequentist approach seeks to find a single 'optimal' value of each

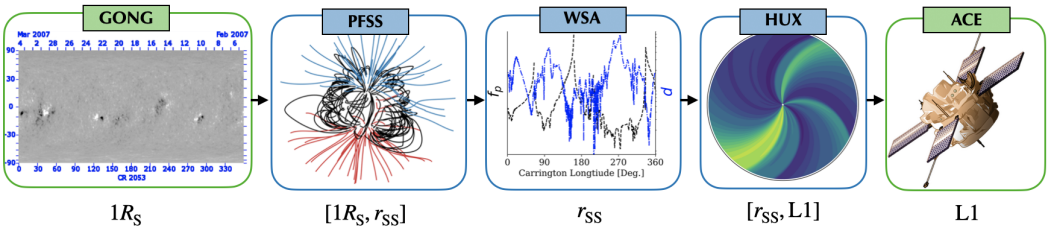

Figure 1. A flowchart of the models and observational data utilized in this study. The GONG and ACE images are adapted from NSO[3] and NASA[4], respectively.

parameter by solving an optimization problem. For example, maximum likelihood estimation (Milton & Arnold, 2003), such that the optimal values of the parameters minimize the difference between the model prediction and observational data. Riley et al. (2015), Reiss et al. (2020), and Kumar and Srivastava (2022) took a frequentist approach to find the optimal parameters in the WSA model. This paper presents a Bayesian approach to learning the uncertain parameters in the PFSS→WSA→HUX model chain. The Bayesian approach views the parameters as random variables and seeks to learn their posterior density. In the Bayesian setting, the solution to the UQ inverse problem is represented by a probability density function of the parameters. In stark contrast, the frequentist approach yields a point estimate. Thus, the Bayesian approach provides a complete picture of the uncertainty associated with the model parameters. Subsequently, relevant point estimates, such as the maximum *a posteriori* (MAP), variance, and mean, can all be computed from the posterior density. Here, we use Markov chain Monte Carlo (MCMC) (Metropolis et al., 1953; Hastings, 1970) to learn the posterior densities of the most influential parameters. In particular, we employ the MCMC affine invariant ensemble sampler (Goodman & Weare, 2010; Foreman-Mackey et al., 2013), which is robust to different scales in the parameters.

The main questions we seek to answer via the proposed UQ framework are: (1) How does parametric uncertainty in the PFSS→WSA→HUX model chain impact the uncertainty in the solar wind velocity predictions near Earth? Can we reduce such uncertainties using Bayesian inference methods? (2) What are the most influential parameters in the model chain? (3) How do the posterior densities of the influential parameters change over time? Is there a clear trend in the posterior evolution? (4) Is the model chain robust to the choice of its parameters? Is it reliable enough to be used for real-time operational forecasting?

This paper is organized as follows. Section 2 describes the models and observational data used in this work. Section 3 discusses variance-based global sensitivity analysis, an algorithm to compute Sobol' sensitivity indices via Monte Carlo integration, and numerical results. In Section 4 we discuss Bayesian inference via MCMC algorithms and numerical results. Section 5 then offers conclusions and an outlook to future work.

2 Ambient Solar Wind Model Chain and Observational Data

We consider the coupling of three well-established models: (1) Potential Field Source Surface (PFSS), (2) Wang-Sheeley-Arge (WSA), and (3) Heliospheric Upwind eXtrapolation (HUX), to predict the ambient solar wind radial velocity near Earth. Reiss et al. (2019, 2020) and Bailey et al. (2021) use a similar chain of models with the addition of the Schatten Current Sheet (SCS) model, developed by Schatten et al. (1969), resulting in the following model chain: PFSS→SCS→WSA→HUX. The SCS model is added to correct the PFSS radial magnetic field latitudinal variations to match Ulysses' observations (Wang & Sheeley, 1995). However, a recent study by Kumar and Srivastava (2022) showed that adding SCS to the chain of models did not necessarily improve the accuracy of the solar wind radial

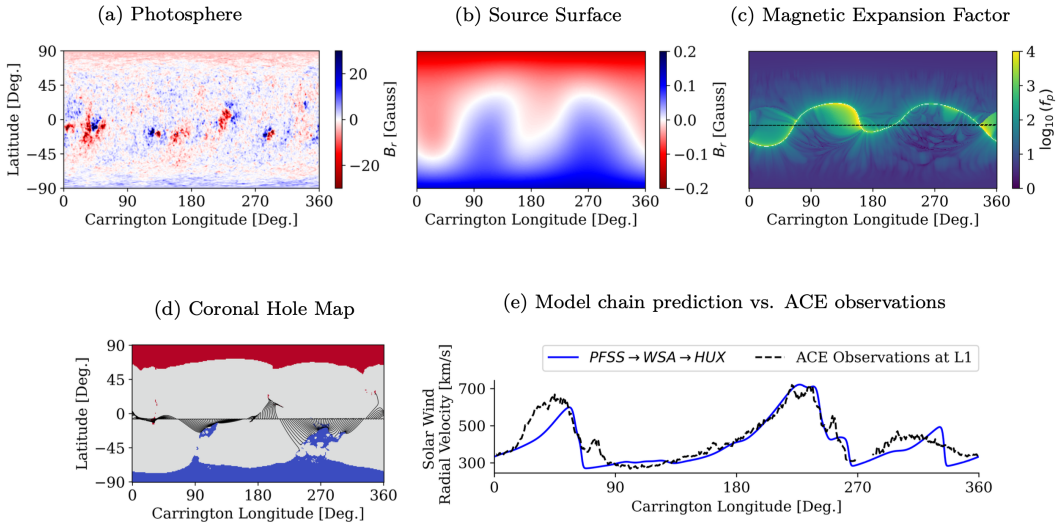

Figure 2. An illustration of different components in PFSS→WSA→HUX model chain during CR 2053. The PFSS radial magnetic field at the lower and upper boundaries is shown in (a) and (b). The lower boundary condition is obtained from GONG synoptic maps and the extrapolated upper boundary is shown at the source surface, which is set to $r_{\rm SS} = 2.5R_{\rm S}$ in this example. The WSA inputs, i.e. the magnetic field expansion factor and coronal hole map, are shown in (c) and (d). The red (blue) coronal hole areas show the negative inward (positive outward) fields. Lastly, (e) shows a comparison of the model chain solar wind radial velocity predictions at L1 with ACE *in-situ* observations. In this example, we set the WSA parameters to $v_0 = 250\frac{\rm km}{\rm s}, v_1 = 945\frac{\rm km}{\rm s}, \alpha = 0.16, \beta = 1, \gamma = 0.6, w = 0.02{\rm rad}, \delta = 1.75, \psi = 3$ and the HUX parameters to $\alpha_{\rm acc} = 0.15, r_h = 50R_{\rm S}$.

velocity predictions at L1 (during 2006-2011). We thus analyze the PFSS→WSA→HUX model chain.

The PFSS model is used to predict the magnetic field in the coronal domain. The PFSS magnetic field solution is then used as an input to the WSA relation, which computes the solar wind radial velocity at the outer boundary of the coronal domain. The WSA results are then set as the initial condition for the HUX model, which extrapolates the solar wind radial velocity into the heliospheric domain. Finally, the model chain solar wind radial velocity predictions are compared with ACE spacecraft *in-situ* observations. We use synoptic magnetograms from Global Oscillation Network Group (GONG) as the inner boundary condition for the PFSS model. A flowchart of the models and data used in this study is shown in Figure 1. The subsequent sections explain the different components of the model chain and observational data in further detail.

2.1 Potential Field Source Surface (PFSS) Model

The PFSS model proposed by Altschuler and Newkirk (1969) and Schatten et al. (1969) solves for the coronal magnetic field $\mathbf{B}(r, \theta, \phi) = [B_r(r, \theta, \phi), B_\theta(r, \theta, \phi), B_\phi(r, \theta, \phi)]$ from the photosphere (the visible surface of the Sun) to the outer radius called the *source surface*. The PFSS model assumes that beyond the source surface, the magnetic field is purely radial, i.e. open magnetic field lines are carried into interplanetary space by the solar wind. Additionally, the PFSS model neglects the coronal electric current density since, above the photosphere, there is a large decrease in particle density and a smaller decrease in magnetic field strength (Kruse et al., 2020); it also assumes that the corona is electrostatic

since during solar minimum, the corona evolves slowly, and features can last for several Carrington rotations (CRs). It is important to mention that some of the above assumptions hold less during specific time periods. For example, during solar maximum, the photospheric field changes more rapidly, challenging the electrostatic assumption. Additionally, Riley et al. (2006) found that the concept of spherical source surface is more reasonable during solar maximum than during solar minimum. These assumptions (coupled with Ampère's law) lead to

$$\nabla \times \mathbf{B} = 0,$$

so that the magnetic field can be described by its potential $\mathbf{B} = -\nabla\Psi$. By combining the potential description with Gauss's law ($\nabla \cdot \mathbf{B} = 0$), we get Laplace's equation

$$\nabla^2 \Psi = 0,$$

subject to the following boundary conditions

$$\begin{aligned} \frac{\partial \Psi}{\partial r}(r = 1R_{\mathrm{S}}, \theta, \phi) &= g(\theta, \phi), \\ \frac{\partial \Psi}{\partial \theta}(r = r_{\mathrm{SS}}, \theta, \phi) &= \frac{\partial \Psi}{\partial \phi}(r = r_{\mathrm{SS}}, \theta, \phi) = 0, \\ \Psi(r, \theta, \phi = 0) &= \Psi(r, \theta, \phi = 2\pi), \end{aligned} \tag{1}$$

where $\theta \in [0, \pi]$ is Carrington colatitude, $\phi \in [0, 2\pi]$ is Carrington longitude, R_{S} denotes solar radii unit of distance which is 695,700km, and approximately 1/215th of an astronomical unit (AU), $r \in [1R_{\mathrm{S}}, r_{\mathrm{SS}}]$ is the radial distance from the center of the Sun, r_{SS} is the source surface height, and $g(\theta, \phi)$ is a given photospheric synoptic map. The PFSS model is typically solved via spherical harmonic expansion or numerical discretization methods (Caplan et al., 2021; Liu et al., 2022; Stansby et al., 2020). We employ the `pfsspy` Python package (version 1.1.2), developed by Stansby et al. (2020), for solving PFSS via finite-difference discretization and for tracing magnetic field lines. The finite-difference discretization is on a rectilinear grid equally spaced in sin(colatitude), longitude, and ln(radius) coordinates, see Stansby et al. (2020) for more details on the solver. In this study, all simulations are performed on a $180 \times 360 \times 100$ grid resolution in sin(colatitude), longitude, and ln(radius), respectively, i.e. we solve for 6.48×10^6 states. As an illustrative example, Figure 2(a) shows the radial magnetic field at the photosphere (inner boundary) for CR 2053 obtained by the GONG synoptic maps (see Section 2.4.1) and Figure 1(b) shows the radial magnetic field results at the source surface (outer boundary), which is set to $r_{\mathrm{SS}} = 2.5R_S$ for this example.

2.2 Wang-Sheeley-Arge (WSA) Model

The WSA model developed by Arge et al. (2004) is a semi-empirical model of the ambient solar wind velocity in the inner-heliosphere, which fuses the Wang-Sheeley (WS) model developed by Wang and Sheeley (1990) with the distance to the coronal hole boundary (DCHB) model developed by Riley et al. (2001). The WSA model (coupled with the MHD Enlil model) is used in operational forecasting at the National Oceanic and Atmospheric Administration (NOAA) Space Weather Prediction Center (Parsons et al., 2011). The WSA model is given by

$$v_{\mathrm{wsa}}(f_p, d, v_0, v_1, \alpha, \beta, \gamma, w, \delta, \psi) = v_0 + \frac{v_1 - v_0}{(1 + f_p)^\alpha} \left(\beta - \gamma \exp\left(- \left(\frac{d}{w} \right)^\delta \right) \right)^\psi,$$

where v_0 and v_1 correspond to the minimum and maximum solar wind velocities, d is the minimum angular distance that an open field footpoint lies from a coronal hole boundary, f_p is the magnetic field expansion factor, and $\alpha, \beta, \gamma, \delta, w, \psi$ are additional tunable parameters.

The magnetic expansion factor f_p is derived from the coronal magnetic field by tracing down field lines from the source surface to the photosphere, namely

$$f_p = \left(\frac{1R_{\rm S}}{r_{\rm SS}}\right)^2 \left|\frac{B_r(1R_{\rm S},\theta_{\rm p},\phi_{\rm p})}{B_r(r_{\rm SS},\theta_{\rm SS},\phi_{\rm SS})}\right|, \tag{2}$$

where $B_r(r,\theta,\phi)$ is the radial magnetic field component, and the subscripts p and SS refer to the field line trace at the photosphere and solar surface, respectively. The distance to the coronal hole boundary d is also derived from the coronal magnetic field solution via a two-step approach. First, the coronal hole regions are identified by tracing field lines from the photosphere to the source surface and detecting the footpoints of all open magnetic field lines, i.e. coronal hole regions. Second, the great-circle angular distance d is computed between the footprints of the open magnetic field lines to the nearest coronal hole boundary. To illustrate these concepts, Figure 2(c) presents the magnetic expansion factor for CR 2053, and the black dashed line shows ACE's spacecraft projected trajectory. Similarly, Figure 2(d) shows the coronal hole map for CR 2053 with ACE's trajectory field line traces, which mainly trace down to low-latitude coronal holes.

2.3 Heliospheric Upwind eXtrapolation (HUX) Model

The two-dimensional HUX model developed by Riley and Lionello (2011) extrapolates the coronal solar wind radial velocity into the heliospheric domain. The HUX model is based on simplified physical assumptions of the fluid momentum equation, which reduces to the following nonlinear scalar homogeneous time-stationary equation

$$-\Omega_{\rm rot}(\theta=\hat{\theta})\frac{\partial v(r,\phi)}{\partial \phi} + v(r,\phi)\frac{\partial v(r,\phi)}{\partial r} = 0, \tag{3}$$

where the independent variables are the radial distance from the Sun r and Carrington longitude ϕ, and the dependent variable is the solar wind radial velocity $v(r,\phi)$. The angular frequency of the Sun's rotation is evaluated at a constant Carrington colatitude $\hat{\theta}$ (Riley & Issan, 2021), which is estimated by $\Omega_{\rm rot}(\theta) = \frac{2\pi}{25.38} - \frac{2.77\pi}{180}\cos\left(\frac{\pi}{2}-\theta\right)^2$. The problem is subject to the boundary condition $v(r_{\rm SS},\phi) = v_{r_{\rm SS}}(\phi)$ and is defined on the longitudinal periodic domain $0 \le \phi \le 2\pi$ and $r \ge r_{\rm SS}$. Riley and Lionello (2011) suggest adding an acceleration boost to the boundary condition (before propagation) to account for the residual acceleration present in the inner heliosphere, i.e.

$$v_{\rm acc}(r_{\rm SS}, v_{r_{\rm SS}}(\phi); \alpha_{\rm acc}, r_h) = \alpha_{\rm acc}(1 - e^{-r_{\rm SS}/r_h})v_{r_{\rm SS}}(\phi), \tag{4}$$

where $v_{r_{\rm SS}}(\phi)$ is the radial velocity at the source surface (obtained from WSA relation), $\alpha_{\rm acc}$ is the acceleration factor, and r_h is the radial location at which the acceleration ends. We discretize Eq. (3) via finite-differencing on a uniform mesh with 600×300 resolution in $\phi \in [0, 2\pi]$ and $r \in [r_{\rm SS}, r_{\rm max}]$, respectively. We set $r_{\rm max}$ to be ACE's maximum radial distance from the Sun for the considered CR. We solve the equation using the first-order upwind scheme, see Issan and Riley (2022) for more details about the numerical scheme and stability requirements. Figure 2(e) shows the coupling of PFSS, WSA, and HUX solar wind speed predictions in comparison to ACE's *in-situ* observations for CR 2053, see Section 2.4.2 for more details about ACE. We set $\hat{\theta}$ to be ACE's mean latitude over a CR and obtain the inner boundary velocity profile by computing the magnetic field expansion and distance to the coronal hole at ACE's projected trajectory (which are inputs in the WSA model). The solar wind velocity at ACE's trajectory is obtained by linearly interpolating the two-dimensional HUX solution along ACE's trajectory.

2.4 Observational Data

2.4.1 Global Oscillations Network Group (GONG) Synoptic Magnetograms

Deployed in 1995, the GONG synoptic magnetograms are produced every hour at GONG's six ground-based sites with identical telescopes. The six sites in California, Hawaii, Australia, India, Spain, and Chile, are distributed worldwide so that the Sun is visible at nearly all times. The line-of-sight full-disk GONG magnetograms are provided every minute by its main instrument known as Fourier Tachometer (Hill, 2018; Harvey et al., 1996). The magnetic field strength (measured in Gauss) is determined spectroscopically using the Zeeman effect. In the presence of a magnetic field, gas spectral lines split into two or more components, and the frequency of the spectral lines depends on the strength of the magnetic field (Moldwin, 2008).

In this study, we use the GONG full CR synoptic magnetograms as the photospheric radial magnetic field $g(\theta, \phi)$ boundary condition for the PFSS model, see Eq. (1), which are publicly available at National Solar Observatory's website[5]. The synoptic maps are calibrated from roughly 8,000-10,000 input full-disk 10-min average magnetograms (Hill, 2018) and are provided at 180×360 resolution in Carrington sin(colatitude) and Carrington longitude, respectively. These synoptic maps are obtained over a full CR and reasonably approximate the solar conditions at quiet times of the cycle when the solar evolution is slow. Figure 2(a) above shows the GONG synoptic map for CR 2053.

2.4.2 Advanced Composition Explorer (ACE) in-situ Solar Wind Measurements

The NASA ACE satellite launched in 1997 is in Lissajous orbit around L1 (one of Earth-Sun gravitational equilibrium points), located about 1.5×10^6 km forward of Earth. The location of ACE gives about 1-hour advance warning of the arrival of space weather events on Earth. The ACE instruments measure the solar wind, interplanetary magnetic field, and high-energy particles. This study uses the solar wind radial velocity *in-situ* measurements provided by ACE's Solar Wind Electron Proton Alpha Monitor (SWEPAM) instrument (McComas et al., 1998). To download the radial velocity data and ACE's trajectory at a 1-hour cadence, we used `HelioPy`, a community-developed Python package (Stansby et al., 2021), for retrieving space physics datasets from NASA's Space Physics Data Facility website[6].

2.5 Model Chain Simulations

The PFSS→WSA→HUX model chain simulations are run on the *Alfvén* server at the University of Colorado SWx-TREC (Space Weather Technology, Research, and Education Center), which is equipped with 2x AMD EPYC 74F3 24-Core processors (3.2 GHz) and a total 2 Tb of RAM. The model chain takes about 16 seconds to simulate on one CPU. We profiled the model chain computations and found that 98% of the total time is spent solving the PFSS model and computing the distance to the coronal hole and magnetic expansion, 1.8% is spent on solving the HUX model and less than a percent is spent on evaluating the WSA model.The sensitivity analysis results required $3 \times 1.3 \times 10^5 = 3.9 \times 10^5$ simulations and the MCMC results required $10 \times 250 \times 2.6 \times 10^4 = 6.5 \times 10^7$ model simulations, i.e. a total of approximately 10,400 CPU hours.

[5] `https://gong.nso.edu/data/magmap/crmap.html`
[6] `https://cdaweb.gsfc.nasa.gov/index.html/`

3 Global Sensitivity Analysis

Variance-based global sensitivity analysis aims to identify the parameters that contribute the most to a given QoI variability, which can be done quantitatively via computing Sobol' sensitivity indices (Sobol', 2001). Parameters with high sensitivity indices are classified as influential, whereas parameters with low sensitivity indices are classified as non-influential. Computing Sobol' sensitivity indices facilitate *a posteriori* parameter dimensionality reduction in subsequent inverse UQ tasks (such as Bayesian inference). This is established by setting non-influential parameters to their nominal values and only considering parametric uncertainty stemming from influential parameters. Parametric dimensionality reduction is often necessary for computationally demanding models and unbiased inverse UQ methods.

3.1 Uncertain Parameters

The PFSS→WSA→HUX model chain has many parameters that are uncertain, inducing uncertainty in the solar wind velocity forecasts near Earth. All uncertain parameters in the model chain are mainly non-physical. We identified a total of eleven uncertain continuous parameters: one parameter in PFSS (source surface height), eight parameters in WSA (numerical parameters), and two parameters in HUX (acceleration parameters). Table 1 lists the uncertain input parameters and their corresponding prior densities. We set all prior densities to be uniform with reasonable ranges determined in previous parametric studies by Lee et al. (2011, §2), Arden et al. (2014, §2.5), Meadors et al. (2020, Eq. 9), Kumar and Srivastava (2022, Table 1), and Riley et al. (2015, Table 1).

The source surface radial height r_{SS} in the PFSS model has intrinsic uncertainties since, in reality, it is non-spherical and is a function of space and time. Lowering the source surface results in more coronal holes, open flux, and strong curvature in the heliospheric current sheet, whereas raising the source surface height results in the opposite effect. Riley et al. (2006) suggested avoiding the strict constraint of a spherical source surface by a detailed comparison of PFSS to MHD models, and Kruse et al. (2020) altered the PFSS model to employ an oblate or prolate elliptical source surface. Arden et al. (2014) show that the source surface has a "breathing" effect of which the canonical $2.5R_S$ source surface, originally suggested by Altschuler and Newkirk (1969), matches measured interplanetary magnetic field (IMF) open flux near Earth during solar maximum, yet extends up to $4R_S$ during solar minimum of solar cycle 23 and the start of cycle 24. A similar study by Lee et al. (2011) found that setting the source surface to $1.8R_S$ matched best the IMF strength during the minimum of solar cycle 23. The optimal source surface heights determined in Arden et al. (2014) and Lee et al. (2011) do not agree and further emphasize the need for additional numerical investigation. Additionally, Lee et al. (2011, Figure 14) and Nikolić (2019, Figure 3) compared the PFSS coronal holes to observed extreme ultraviolet synoptic images, their results suggest $1.5 - 1.8R_S$ for the source surface during CR 2060. Similar to our study, Meadors et al. (2020) also considers the source surface as an uncertain input parameter and learns its density via particle filtering and WIND spacecraft observations. Based on Lee et al. (2011, §2), Arden et al. (2014, §2.5) and Meadors et al. (2020, Eq. 9), we allow the source surface to vary from $1.5R_{\mathrm{S}}$ to $4R_{\mathrm{S}}$.

The eight numerical parameters of the WSA model, $v_0, v_1, \alpha, \beta, \gamma, \delta, w, \psi$, similar to the source surface, cannot be directly measured and are usually adjusted for different observatories, e.g. Wilcox solar observatories and GONG (Riley et al., 2015). Additionally, Riley et al. (2015) and Kumar and Srivastava (2022) showed that the optimal parameter can vary greatly from one CR to the next. It is, therefore, important to understand the uncertainties in the WSA parameters and their impact on predicted solar wind speed near Earth. We set the eight parameter ranges based on previous parametric studies by Riley et al. (2015, Table 1) and Kumar and Srivastava (2022, Table 1).

Table 1. The eleven uncertain continuous parameters in the PFSS→WSA→HUX model chain are modeled with uniform priors with physically meaningful ranges taken from previous parametric studies by Lee et al. (2011, §2), Arden et al. (2014, §2.5), Meadors et al. (2020, Eq. 9), Kumar and Srivastava (2022, Table 1), and Riley et al. (2015, Table 1).

Parameter	Model	Description	Prior Range	Nominal Value
r_{SS} $[R_{\mathrm{S}}]$	PFSS	source surface height	$[1.5, 4]$	2.5
v_0 $[\frac{\mathrm{km}}{\mathrm{s}}]$	WSA	minimum velocity	$[200, 400]$	250
v_1 $[\frac{\mathrm{km}}{\mathrm{s}}]$	WSA	maximum velocity	$[550, 950]$	750
α	WSA	numerical parameter	$[0.05, 0.5]$	0.1
β	WSA	numerical parameter	$[1, 1.75]$	1
w [rad]	WSA	numerical parameter	$[0.01, 0.4]$	0.02
γ	WSA	numerical parameter	$[0.06, 0.9]$	0.9
δ	WSA	numerical parameter	$[1, 5]$	1.75
ψ	WSA	numerical parameter	$[3, 4]$	3
α_{acc}	HUX	acceleration factor	$[0, 0.5]$	0.15
r_h $[R_{\mathrm{S}}]$	HUX	radial location at which the acceleration ends	$[30, 60]$	50

The HUX model has two free parameters α_{acc} and r_h in the acceleration boost term, see Eq. (4). Riley and Lionello (2011) suggest setting $\alpha_{\mathrm{acc}} = 0.15$ and $r_h = 50R_{\mathrm{S}}$. A recent study by Riley and Issan (2021) compared HUX to three-dimensional MHD velocity predictions and found the optimal α_{acc} and r_h via nonlinear least-squares optimization for a few CRs spanning from CR 2029 to CR 2231. They found that the average optimal α_{acc} and r_h are 0.16 and $52.6R_S$, respectively. Riley and Issan (2021) took a frequentist approach to find the optimal HUX parameters. In this study, we formulate the inference problem using the Bayesian approach, which provides a complete picture of parametric uncertainty in the form of a non-parametric posterior density. From this, one can compute any relevant estimates, such as the MAP, mode, etc. We allow the two HUX parameters to vary based on physically reasonable ranges specified in Table 1.

3.2 Sobol' Indices

To introduce the notion of global sensitivity indices, let $(\Omega, \mathcal{F}, \mathbb{P})$ be a probability space with sample space Ω, σ-algebra $\mathcal{F}$, and the probability measure $\mathbb{P}$, where $X : \Omega \to \mathcal{X}$ is a random vector with its entries being independent random variables X_i for $i = 1, \dots d$. We denote with $x = X(\omega)$ a sample (realization) of the random vector X for a given event $\omega \in \Omega$. From the independence assumption, the joint probability density function (pdf) $\pi(x)$ is the product of the marginals, i.e. $\pi(x) = \pi_1(x_1)\pi_2(x_2)\cdots\pi_d(x_d)$. We consider a generic model $f : \mathcal{X} \to \mathcal{Y}$ that maps a d-dimensional input parameter $x = [x_1, x_2, \dots, x_d]^\top \in \mathcal{X} \subseteq \mathbb{R}^d$ to a scalar QoI $y \in \mathcal{Y} \subseteq \mathbb{R}$. We assume that f is square-integrable with respect to π, such that the expectation (mean) $\mathbb{E}[f(X)] = \int_{\mathbb{R}^d} f(x)\pi(x)\mathrm{d}x$ and variance $\mathbb{V}\mathrm{ar}[f(X)] = \int_{\mathbb{R}^d} \left(f(x) - \mathbb{E}[f(x)]\right)^2 \pi(x)\mathrm{d}x$ of the QoI are both finite.

Definition 1 (Sobol' Indices) The *first-order Sobol' sensitivity indices* measure the main variance contribution due to the ith random input parameter, such that

$$S_i \coloneqq \frac{\mathbb{V}\mathrm{ar}_{X_i}[\mathbb{E}_{X_{\sim i}}(f(X)|X_i)]}{\mathbb{V}\mathrm{ar}[f(X)]}, \qquad i = 1, \ldots, d, \tag{5}$$

where $\mathbb{V}\mathrm{ar}_{X_i}$ denotes the variance with respect to only the X_i random input parameter, $\mathbb{V}\mathrm{ar}$ without subscript denotes variance involving all parameters, and $X_{\sim i}$ denotes all random input parameters but X_i. The *second-order Sobol' sensitivity indices* measure the secondary variance contribution due to the interaction of the ith and jth parameters (where $i \neq j$), such that

$$S_{ij} \coloneqq \frac{\mathbb{V}\mathrm{ar}_{X_i,X_j}[\mathbb{E}_{X_{\sim i,j}}(f(X)|X_i, X_j)]}{\mathbb{V}\mathrm{ar}[f(X)]} - S_i - S_j.$$

The *total-order Sobol' sensitivity indices* measure the total variance contributions of the ith parameter, such that

$$T_i \coloneqq S_i + \sum_{j=1}^{d} S_{ij} + \text{H.O.T.} = 1 - \frac{\mathbb{V}\mathrm{ar}_{X_{\sim i}}[\mathbb{E}_{X_i}(f(X)|X_{\sim i})]}{\mathbb{V}\mathrm{ar}[f(X)]} = \frac{\mathbb{E}_{X_{\sim i}}[\mathbb{V}\mathrm{ar}_{X_i}(f(X)|X_{\sim i})]}{\mathbb{V}\mathrm{ar}[f(X)]}, \tag{6}$$

where H.O.T. refers to higher-order terms. The first, second, and higher-order indices sum up to 1, such that

$$\sum_{i=1}^{d} S_i + \sum_{i=1}^{d} \sum_{j=2, j>i}^{d} S_{ij} + \cdots + S_{12\ldots d} = 1.$$

Notice that if the total-order index $T_i \approx 0$, then $\mathbb{E}_{X_{\sim i}}[\mathbb{V}\mathrm{ar}_{X_i}(f(X)|X_{\sim i})] \approx 0$, which, by the non-negativity of the variance operator, implies that $\mathbb{V}\mathrm{ar}_{X_i}(f(X)|X_{\sim i}) \approx 0$. Therefore, if $T_i \approx 0$, the uncertainty in X_i hardly influences the variance of the QoI, and X_i can be deemed as non-influential.

Sobol' sensitivity indices can not be computed in closed form except for QoIs that are integrable with respect to π (the joint probability of the uncertain parameters X). Appendix A shows that the sensitivity indices can be computed analytically for the simple Wang-Sheeley model (Wang & Sheeley, 1990). However, the QoIs we consider (like most model QoIs arising from simulations of complex systems) are not integrable with respect to π. Thus, we need to approximate the indices numerically.

3.3 Estimating Sobol' Indices via Monte Carlo Integration

The first- and total-order Sobol' sensitivity indices described in Eqns. (5) and (6) can be estimated via Monte Carlo (MC) integration, which requires $N(d+2)$ model evaluations, where N is the number of independent samples of X and d is the number of uncertain parameters. Since each model evaluation is independent of the other, the MC model evaluations can be easily computed in parallel. The four-step algorithm of Saltelli (2002), which is based on Sobol' (2001) original work, is implemented as follows:

1. Draw $2N$ quasi-random samples of the random vector X and store them as

$$A = \begin{bmatrix} x_1^{(1)} & \ldots & x_d^{(1)} \\ \vdots & & \vdots \\ x_1^{(N)} & \ldots & x_d^{(N)} \end{bmatrix} \in \mathbb{R}^{N\times d} \qquad \text{and} \qquad B = \begin{bmatrix} x_1^{(N+1)} & \ldots & x_d^{(N+1)} \\ \vdots & & \vdots \\ x_1^{(2N)} & \ldots & x_d^{(2N)} \end{bmatrix} \in \mathbb{R}^{N\times d},$$

   where $x_i^{(j)}$ denotes the ith entry and jth sample of X. Quasi-MC methods generate near-random samples that aim to distribute well over the parameter space. These sampling strategies usually result in a faster rate of convergence in MC inte-

gration. We use Latin hypercube sampling developed by McKay et al. (1979). Other common quasi-random low-discrepancy sequences are Sobol' (Sobol', 1967) and Halton (Halton, 1960).

2. Define matrices $C^{(i)}$ for $i = 1, 2, \ldots, d$, which are a copy of B except the ith column is replaced by $A(:, i)$, the ith column of A, so that

$$C^{(i)} = \begin{bmatrix} | & & | & & | \\ B(:,1) & \ldots & A(:,i) & \ldots & B(:,d) \\ | & & | & & | \end{bmatrix} \in \mathbb{R}^{N \times d}, \qquad i = 1, \ldots, d.$$

3. Evaluate the QoI for each row of the matrices $A, B, C^{(i)}$, denoted as $A(j,:)$, $B(j,:)$, $C^{(i)}(j,:)$, i.e.

$$y_A^{(j)} = f(A(j,:)) \in \mathbb{R}, \qquad y_B^{(j)} = f(B(j,:)) \in \mathbb{R} \qquad \text{and} \qquad y_{C^{(i)}}^{(j)} = f(C^{(i)}(j,:)) \in \mathbb{R},$$

for $j = 1, \ldots, N$. The evaluation of y_A and y_B requires $2N$ model evaluations, whereas the evaluation of $y_{C^{(i)}}$ requires $d \cdot N$ model evaluations, which results in a total of $N(d+2)$ model evaluations.

4. Estimate using MC integration the first-order S_i and total-order T_i sensitivity indices for $i = 1, \ldots, d$. We use the unbiased Janon/Monod's estimator (Janon et al., 2014; Monod et al., 2006), such that

$$S_i \approx \frac{\frac{1}{N}\sum_{j=1}^{N} y_A^{(j)} y_{C^{(i)}}^{(j)} - \left(\frac{1}{N}\sum_{j=1}^{N} y_A^{(j)}\right)\left(\frac{1}{N}\sum_{j=1}^{N} y_{C^{(i)}}^{(j)}\right)}{\frac{1}{N}\sum_{j=1}^{N}\left(y_A^{(j)}\right)^2 - \left(\frac{1}{N}\sum_{j=1}^{N} y_A^{(j)}\right)^2},$$

$$T_i \approx 1 - \frac{\frac{1}{N}\sum_{j=1}^{N} y_B^{(j)} y_{C^{(i)}}^{(j)} - \left(\frac{1}{N}\sum_{j=1}^{N}\left(\frac{y_B^{(j)} + y_{C^{(i)}}^{(j)}}{2}\right)\right)^2}{\frac{1}{2N}\sum_{j=1}^{N}\left(\left(y_B^{(j)}\right)^2 + \left(y_{C^{(i)}}^{(j)}\right)^2\right) - \left(\frac{1}{N}\sum_{j=1}^{N}\left(\frac{y_B^{(j)} + y_{C^{(i)}}^{(j)}}{2}\right)\right)^2}.$$

The algorithm intuition can be explained as follows. The first-order sensitivity estimation is based on the product of y_A and $y_{C^{(i)}}$, which multiplies the QoI with input A and the QoI with input $C^{(i)}$ where all parameters except X_i have been re-sampled. Intuitively, if X_i is influential then y_A and $y_{C^{(i)}}$ are correlated and S_i is large. We can intuit the estimation of the total-order indices T_i in a similar way. The product of y_B and $y_{C^{(i)}}$ multiplies the QoI with input B and the QoI with input $C^{(i)}$ where we only re-sample X_i. Thus, if X_i is influential then y_B and $y_{C^{(i)}}$ are not correlated and T_i is large.

There are many other MC Sobol' sensitivity indices estimators, see Puy et al. (2022) for a comprehensive comparison. Saltelli's (Saltelli, 2002) and Jansen's (Jansen, 1999) estimators are also commonly used estimators. We compared the three estimators and found that Janon/Monod's estimator resulted in faster convergence for our study.

3.4 Global Sensitivity Analysis Numerical Results

We perform global sensitivity analysis using the PFSS→WSA→HUX model chain for CR 2048 (September 21st, 2006 to October 18th, 2006), CR 2053 (February 4th, 2007 to March 4th, 2007), and CR 2058 (June 21st, 2007 to July 18th, 2007). The three CRs occurred during the declining phase of solar cycle 23. The eleven model input parameters are listed in Table 1 and are described in Section 3.1. We use $N = 10^4$ Latin Hypercube samples (McKay et al., 1979) to estimate the Sobol' sensitivity indices via MC integration (Section 3.3), which requires $N(d+2) = 1.3 \times 10^5$ model evaluations for each CR. We consider two quantities of interest: the RMSE between ACE velocity measurements and the model predictions at L1 and longitude-dependent model predictions at L1 (independent of ACE observations). The results are discussed in the following subsections.

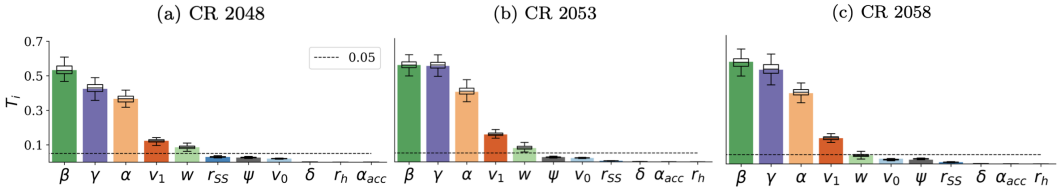

Figure 3. The total-order indices T_i of the RMSE between the model chain and ACE observations are shown for (a) CR 2048, (b) CR 2053, and (c) CR 2058. The box plot for each index shows the uncertainty in the index estimate using bootstrapping with $N = 3 \times 10^3$ samples and 100 replications. The box plots display the range between the first and third quartiles, with a middle line indicating the median. The whiskers represent the span from the minimum to maximum estimates. The results show that $r_{\text{SS}}, \psi, \delta, v_0, r_h, \alpha_{\text{acc}}$ are non-influential as their total-order indices are lower than 0.05 (shown in dashed black horizontal line).

3.4.1 Sobol' Indices for RMSE

The QoI $f(X)$ for which we compute the Sobol' sensitivity indices is the root mean squared error (RMSE) between the model chain solar wind radial velocity prediction at L1 and ACE at 1-hour cadence observations. Figure 3 shows the total-order indices for CR 2048, CR 2053, and CR 2058. The total-order indices for all three CRs have the same ordering for the five most influential parameters, i.e. $\beta, \gamma, \alpha, v_1, w$ (listed in descending order). The five most influential parameters are all WSA model parameters. The other six parameters $r_{\text{SS}}, \psi, v_0, \delta, r_h, \alpha_{\text{acc}}$ are deemed as non-influential since their total-order indices are less than 0.05. We also estimate the uncertainty in the estimated total-order indices by using bootstrapping with $N = 3 \times 10^3$ samples and 100 replications. The box plots for each index are shown in Figure 3. The uncertainty in the estimated total-order indices does not influence the classification between influential and non-influential parameters. The total-order indices show that six out of the eleven uncertain parameters are non-influential, and subsequently, they hardly contribute to the predicted solar wind radial velocity variability at L1. We, therefore, set the six non-influential parameters to their fixed nominal values (see Table 1) in the subsequent Bayesian inference, which facilitates *a posteriori* dimensionality reduction and significant computational speed up for performing MCMC.

Figure 4(a) shows an ensemble of the global sensitivity analysis model evaluations for CR 2053. We plot the median and 50% and 95% credible interval of the 1.3×10^5 model evaluations used to compute the sensitivity indices (which were constructed via prior density samples). A *credible interval* is an interval within which the ensemble members fall with a particular probability. The 95% credible interval shown in Figure 4(a) spans an excessively large range and includes non-physical solutions (for example, solar wind radial velocity at $1800 \frac{\text{km}}{\text{s}}$). This is because the uncertainties in the model chain parameters highly influence the solar wind velocity predictions at L1. We aim to reduce such large parametric uncertainties via Bayesian inference; see Section 4. Figure 4(b) and Figure 4(c) show histograms of the RMSE and Pearson correlation coefficient (PCC) between the global sensitivity analysis simulations in comparison to ACE observations for CR 2053. The histograms show that the RMSE mean is $217.2 \frac{\text{km}}{\text{s}}$ and the PCC mean is 0.5. Also, the RMSE maximum *a posteriori* (MAP) is $101.5 \frac{\text{km}}{\text{s}}$ and the PCC MAP is 0.71. By reducing the uncertainty in the model parameters, we expect the ensemble to be more accurate.

3.4.2 Longitude-Dependent Sobol' Indices

We define longitude-dependent (or time-dependent) QoIs, which are the solar wind radial velocity predictions at L1 at a 1-hour cadence. In contrast to the RMSE indices,

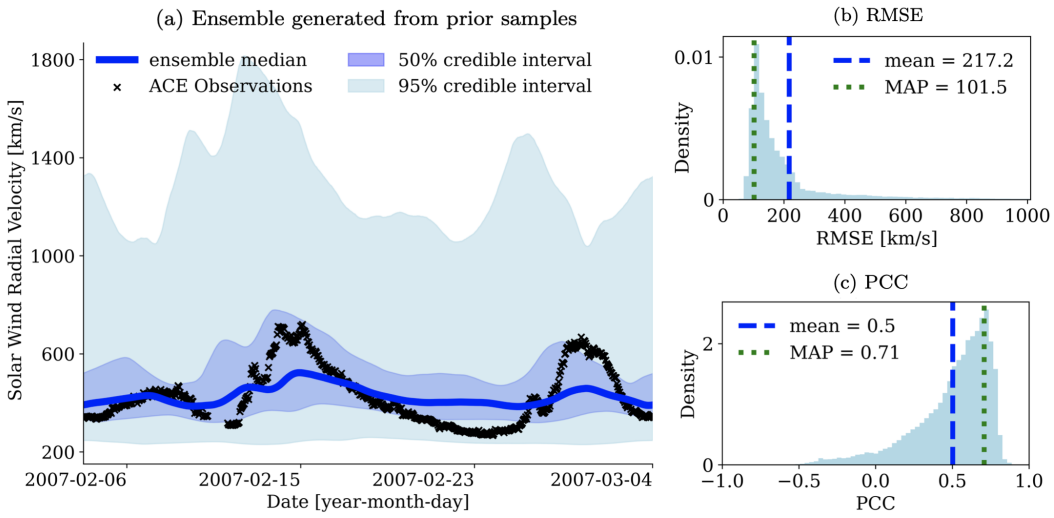

Figure 4. (a) Ensemble generated from prior samples of the global sensitivity analysis model evaluations for CR 2053. The credible interval shows that parametric uncertainty in the model chain results in very high uncertainty in the solar wind radial velocity predictions at L1. A histogram of the ensemble RMSE and PCC are shown in (b) and (c), respectively.

defined in Subsection 3.4.1, the longitude-dependent QoIs are independent of ACE observations. Figure 5 presents the seven largest first-order S_i and total-order T_i indices as a function of Carrington longitude for CR 2048, CR 2053, and CR 2058. We do not plot the first- and total-order indices of $\psi, \delta, \alpha_{\text{acc}}, r_h$ since their maximum indices (in longitude) are less than 0.05. The five most influential parameters during all three CRs are $\beta, \gamma, \alpha, v_1, w$, which agree with the RMSE indices results, see Figure 3. The first-order indices are significantly smaller than the total-order indices, which indicates that higher-order interactions between parameters influence the predicted solar wind velocity variability. Additionally, the influence of w, the width over which the solar wind ramps up from low- to high-speed flow at coronal-hole boundaries, is mainly around a small longitudinal region. For example, during CR 2053, w is only influential from approximately 190° to 280°. We suspect this is because ACE's footprints lie closer to the center of a low-latitude coronal hole at approximately 250° to 310°, see Figure 2(d). The large distance to coronal hole boundary d corresponds to high solar wind speed in this region, which is then advected to 190° to 280° at L1 (at $\frac{1}{v}$ speed, see Eq. (3)). Thus, w seems to be influential only in regions where d, the distance to the coronal hole boundary, in the WSA relation is large.

4 Bayesian Inference via Markov Chain Monte Carlo Sampling

After identifying the set of influential parameters via variance-based global sensitivity analysis, our goal is to learn the uncertainties of such influential parameters, which we achieve through Bayesian inference. Bayesian parameter estimation leverages Bayes' theorem to learn the pdf of uncertain model parameters given observational data. Samples from such pdfs can be directly obtained using Markov chain Monte Carlo (MCMC) algorithms. These samples are then used to generate an ensemble prediction to quantify and reduce the effect of the parametric uncertainty on the QoI. The following subsections introduce Bayesian inference and MCMC sampling.

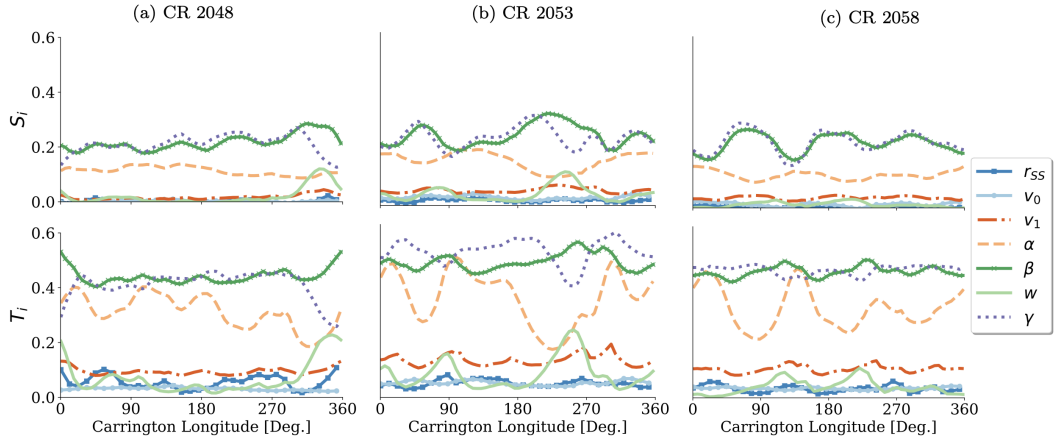

Figure 5. Longitude-dependent (top) first-order S_i and (bottom) total-order indices T_i for (a) CR 2048, (b) CR 2053, and (c) CR 2058. We do not plot the indices of $\psi, \delta, \alpha_{\text{acc}}, r_h$ since their maximum first-order and total-order indices (in longitude) are less than 0.05. The parameters $\beta, \gamma, \alpha, v_1$ are the most influential across all longitudinal locations, whereas w seems to be more longitudinal (or time) dependent. For example, during CR 2048, w is only influential from approximately 280° to 360° in longitude.

4.1 Bayesian Parameter Estimation

The philosophy behind Bayesian statistics is that the model parameters are random variables with an unknown pdf. This differs from the frequentist perspective, where the parameters are assumed deterministic but unknown. In the Bayesian setting, we seek to estimate the pdf of model influential parameters X given a parameter-dependent QoI $f(\cdot)$ (e.g. solar wind radial velocity at L1) and measurements of the QoI $z = \{z_1, z_2, \ldots, z_n\}$ (e.g. ACE radial velocity measurements) taken at time instances $t_1 < t_2 < \ldots < t_n$ (e.g., at a 1-hour cadence). In other words, we aim to estimate the conditional pdf $\pi(x|z)$, which is referred to as the *posterior density* or simply *posterior*. The posterior density can be evaluated via Bayes' rule:

$$\pi(x|z) = \frac{\pi(z|x)\pi(x)}{\pi(z)} = \frac{\pi(z|x)\pi(x)}{\int_{\mathbb{R}^d} \pi(z|x)\pi(x)\mathrm{d}x} \propto \pi(z|x)\pi(x),$$

where $\pi(x)$ is the *prior*, $\pi(z|x)$ is the *likelihood*, and $\pi(z)$ is the *evidence* (also referred to as the marginal likelihood or normalizing constant). The parameters x are samples of the random variable X, and the observations z_i are samples of the random variable Z_i. Most often, the evidence can not be properly defined, so we estimate the posterior up to a normalizing constant. The posterior density can be continuously refined as more measurements are included.

The prior density $\pi(x)$ is chosen based on physically meaningful ranges and previous studies in the literature; see Table 1 for the list of the uniform prior densities used in this study. Generally, the priors are not restricted to uniform densities and may weigh favorable values more heavily. However, if prior knowledge is of questionable accuracy, it is better to use non-informative priors (Smith, 2013, §8.1).

We assume that the QoI of the model and measurements are related via

$$Z_i = f(X; t_i) + \epsilon_i, \qquad i = 1, \ldots, n, \tag{7}$$

where Z_i is a random variable representing the measurements at time instance t_i, $f(X;t_i)$ is the QoI at time instance t_i and ϵ_i is a random variable representing the discrepancies between the QoI and measurements. Here, we model ϵ_i as a Gaussian random variable with zero mean and standard deviation $\sigma \in \mathbb{R}_+$. We note that the model discrepancies and measurement noise are modeled as additive and mutually independent of X. Thus, by the assumption of Gaussian additive error and independence of measurements, we can write the likelihood as

$$\pi(z|x) = \prod_{i=1}^{n} \frac{1}{\sqrt{2\pi\sigma^2}} \exp\left(-\frac{1}{2\sigma^2}\left[z_i - f(x;t_i)\right]^2\right) \propto \exp\left(-\frac{1}{2\sigma^2}\sum_{i=1}^{n}\left[z_i - f(x;t_i)\right]^2\right).$$

Although we derived an expression for the prior and likelihood densities, we can not directly sample from the posterior density since the evidence (or normalizing constant) remains unknown. To overcome this issue, MCMC algorithms enable sampling from arbitrary pdfs and allow for the unbiased estimation of the posterior density, mean, and variance.

4.2 Markov Chain Monte Carlo Sampling

MCMC algorithms generate samples from an arbitrary target pdf (such as posterior pdf) by generating a random walk in the parameter space that draws a representative set of samples from the target pdf. The random walk is a Markov chain, with the property that each sample only depends on the position of the previous sample. MCMC algorithms converge to the exact target pdf as the number of samples increases. This convergence property is established by the ergodicity property of MCMC, which requires the Markov chain to be aperiodic, irreducible, and reversible with respect to the target pdf (Roberts & Rosenthal, 2004).

The first and most frequently used MCMC algorithm is the Metropolis-Hastings algorithm (Metropolis et al., 1953; Hastings, 1970) developed at Los Alamos National Laboratory. The Metropolis–Hastings algorithm generates samples from an arbitrary pdf iteratively. The samples are drawn from a proposal density which is chosen *a priori* and depends on the position of the previous sample of the Markov chain. A proposed sample is then accepted or rejected with some probability. If accepted, the proposed sample is appended to the Markov chain and used to generate the next sample; otherwise, if rejected, the proposed sample is discarded, and the previous sample is appended to the Markov chain. A common choice of proposal density is the Gaussian distribution centered at the previous sample location.

4.2.1 Affine Invariant Ensemble Sampler (AIES)

In this study, we use the affine invariant ensemble sampler (AIES) developed by (Goodman & Weare, 2010), which is an adaptive ensemble extension of the original Metropolis-Hastings sampler (Metropolis et al., 1953; Hastings, 1970). Instead of evolving a single Markov chain, AIES evolves an ensemble of chains, called *walkers*, in parameter space. AIES is invariant under an affine transformation of the parameter space, which is particularly appealing for problems where the parameter scales vary by several orders of magnitude, i.e. highly anisotropic target pdfs. AIES can transform anisotropic pdfs to isotropic pdfs with an affine transformation, which is much easier to sample from. Additionally, other MCMC samplers typically require tuning many sampler hyperparameters; for example, Metropolis-Hastings has d^2 hyperparameters parameters where d is the number of uncertain parameters (entries of the Gaussian proposal distribution covariance). Such tuning is often infeasible when the posterior evaluations are computationally demanding, as is the case in many space weather applications. AIES addresses this challenge by having only two hyperparameters in the stretch move (Goodman & Weare, 2010). One hyperparameter in AIES is the number of walkers L, which is required to be greater than double the number of uncertain parameters

$L \geq 2d + 1$, and the other hyperparameter denoted by a is related to the stretch move, which we explain next.

The AIES stretch move is described as follows. Consider an ensemble of walkers $\{\Upsilon_1(\ell), \ldots, \Upsilon_L(\ell)\}$, where $\ell = 1, \ldots, M$ is the iteration index and L is the number of walkers. The proposed next step for an arbitrary walker $\Upsilon_k(\ell)$ is given by

$$\Upsilon_k(\ell + 1) = \Upsilon_j(\ell) + S\left(\Upsilon_k(\ell) - \Upsilon_j(\ell)\right)$$

where $\Upsilon_j(\ell)$ is a complementary walker in the ensemble chosen at random (where $j \neq k$), S is a random variable with density $g(s)$ that satisfies $g\left(\frac{1}{s}\right) = sg\left(s\right)$. An example of such a density, proposed by Goodman and Weare (2010) and implemented in the `emcee` Python package (Foreman-Mackey et al., 2013), is

$$g(s) = \begin{cases} \frac{1}{\sqrt{s}} & s \in [\frac{1}{a}, a] \\ 0 & \text{otherwise,} \end{cases} \tag{8}$$

where $a > 1$ can be adjusted to improve the sampler's performance and is typically set to $a = 2$. Thus, the proposed next step for a given walker lies on a straight line connecting the walker's current location and another random walker in the ensemble. The acceptance probability of the next proposed step is

$$\mathbb{P}\left(\Upsilon_k(\ell + 1) | \Upsilon_k(\ell)\right) = \min\left(1, S^{d-1} \frac{\pi(\Upsilon_k(\ell + 1))}{\pi(\Upsilon_k(\ell))}\right),$$

where S is the random variable with density defined in Eq. (8), d is the number of uncertain parameters, and π is the target pdf. If the proposal is rejected, then $\Upsilon_k(\ell + 1) = \Upsilon_k(\ell)$.

In this study, we use the Python implementation of AIES, i.e. the `emcee` package (version 3.1.4) developed by Foreman-Mackey et al. (2013), with the stretch move, $a = 2$, and $L = 250$ walkers. We initialize the walkers by randomly sampling a Gaussian density with the mean set to the prior mean and standard deviation set to 10^{-2} times the prior range.

4.2.2 Markov Chain Monte Carlo Burn-in

MCMC *burn-in* refers to the period when a Markov chain exhibits initial transient behavior unrepresentative of the target pdf. It is therefore recommended to disregard the first few iterations at the beginning of the Markov chain (Smith, 2013, §8.4). Burn-in is typically an artifact of selecting a low-probability initial condition and can also be thought of as a way to find a better initial condition. The burn-in length can be chosen by detecting the iteration where the target pdf evaluations start to plateau, which can be assessed visually (or statistically) by monitoring the likelihood evaluations and the marginal paths associated with each parameter as a function of MCMC iterations. We found that after 10^3 iterations, the likelihood evaluations began to plateau, meaning the Markov chains entered a region of high probability. We, therefore, disregard the first 10^3 samples in each walker, which we consider as the burn-in period.

4.2.3 Markov Chain Monte Carlo Convergence Assessment

Estimating the mean of a Markov chain (or an ensemble of Markov chains) is challenging since its samples are not independent and identically distributed (i.i.d.). This is because—by definition—each sample depends on the previous sample in a Markov chain. Therefore, samples drawn close to each other tend to be correlated. The MC mean estimator of an ensemble of Markov chains with L walkers and M iterations is an unbiased estimator,

620 i.e.

621 $$\hat{\mu} = \frac{1}{M}\sum_{\ell=1}^{M}\left(\frac{1}{L}\sum_{j=1}^{L}\Upsilon_j(\ell)\right) \qquad \text{with} \qquad \mathbb{V}\text{ar}[\hat{\mu}] = \frac{\tau}{LM}\mathbb{V}\text{ar}[\Upsilon],$$

622 where τ is the *integrated autocorrelation time* (IAT)

623 $$\tau = \sum_{\ell=-\infty}^{\infty}\frac{C(\ell)}{C(0)} = 1 + 2\sum_{\ell=1}^{\infty}\frac{C(\ell)}{C(0)}$$

624 and $C(\ell) = \lim_{h\to\infty}\mathbb{C}\text{ov}[\Upsilon(\ell+h), \Upsilon(h)]$ is the lag-ℓ autocovariance function. In practice,
625 the IAT and the autocovariance function are estimated using a finite Markov chain of length
626 M, see Foreman-Mackey et al. (2013) for a more detailed discussion. The larger the IAT,
627 the more samples are needed to converge to the target pdf. In this study, we run the chains
628 until their length M is at least 50 times the maximum IAT (which is computed for each
629 parameter) as suggested by Foreman-Mackey et al. (2013) and compute the estimated IAT
630 using the Python `emcee` package (Foreman-Mackey et al., 2013).

631 ### 4.3 Markov Chain Monte Carlo Numerical Results

632 We use the AIES sampler (described in Section 4.2.1) to uncover the posterior density
633 of the five most influential parameters $\beta, \gamma, \alpha, v_1, w$, for CR 2048 to CR 2058 (spanning
634 from September 21st, 2006 to July 18th, 2007). We exclude CR 2051 since, during this
635 time period, three CMEs reached L1, and the PFSS→WSA→HUX model chain does not
636 account for transient events such as CMEs. We assume in Eq. (7) that the model chain
637 solar wind radial velocity predictions at L1 and ACE measurements (at 1-hour cadence) are
638 related via Gaussian error with mean zero and standard deviation $\sigma = 80\frac{\text{km}}{\text{s}}$. The standard
639 deviation is chosen from previous parametric studies by Reiss et al. (2020, Table 1) and
640 Kumar and Srivastava (2022, Figure 8). The posteriors are approximated with 2.6×10^4
641 MCMC iterations, 10^3 iterations excluded for burn-in, and $L = 250$ walkers, resulting in
642 $M = 6.25 \times 10^6$ MCMC posterior samples per CR.

643 #### *4.3.1 Markov Chain Monte Carlo Posterior Densities*

644 The posterior densities for CR 2052 and CR 2053 in one- and two-dimensional pro-
645 jected parameter space are shown in Figure 6. It is apparent that the marginal posterior
646 of v_1 is uniformly distributed (resembling the prior density in Table 1), meaning that v_1
647 is highly uncertain and can take any value in the prior range with equal probability. This
648 means that the likelihood function is flat in the v_1 direction, i.e. v_1 may not be identifiable
649 from ACE observations. The corner plot shows that β and v_1 are negatively correlated.
650 Note that the marginal posteriors of parameters α and β have little to no support overlap
651 in CR 2052 and CR 2053. This suggests that such parameters are difficult to predict in
652 advance.

653 The marginal posterior densities for CR 2048 to CR 2058 (excluding CR 2051) are
654 shown in Figure 7, which indicates that the posterior densities evolve from one CR to the
655 next in a non-predictable fashion. For example, the marginalized posterior of α has relatively
656 small support that varies randomly from one CR to the next. We also notice that the MAP,
657 shown in dashed vertical lines, changes greatly from one CR to the next, which agrees with
658 the previous parametric studies by Kumar and Srivastava (2022) and Riley et al. (2015).
659 Since the posterior densities vary greatly from one CR to the next, it is not possible to use
660 the posterior samples from a given CR to create an accurate ensemble prediction of the next
661 CR (in contrast to the adaptive-WSA method proposed by Reiss et al. (2020)). If the model
662 chain is used for re-analysis studies, we recommend using the proposed UQ framework to
663 generate accurate ensembles. The ensembles generated from the MCMC posterior samples
664 will be highly accurate as the parameter posteriors are learned using observational data at L1

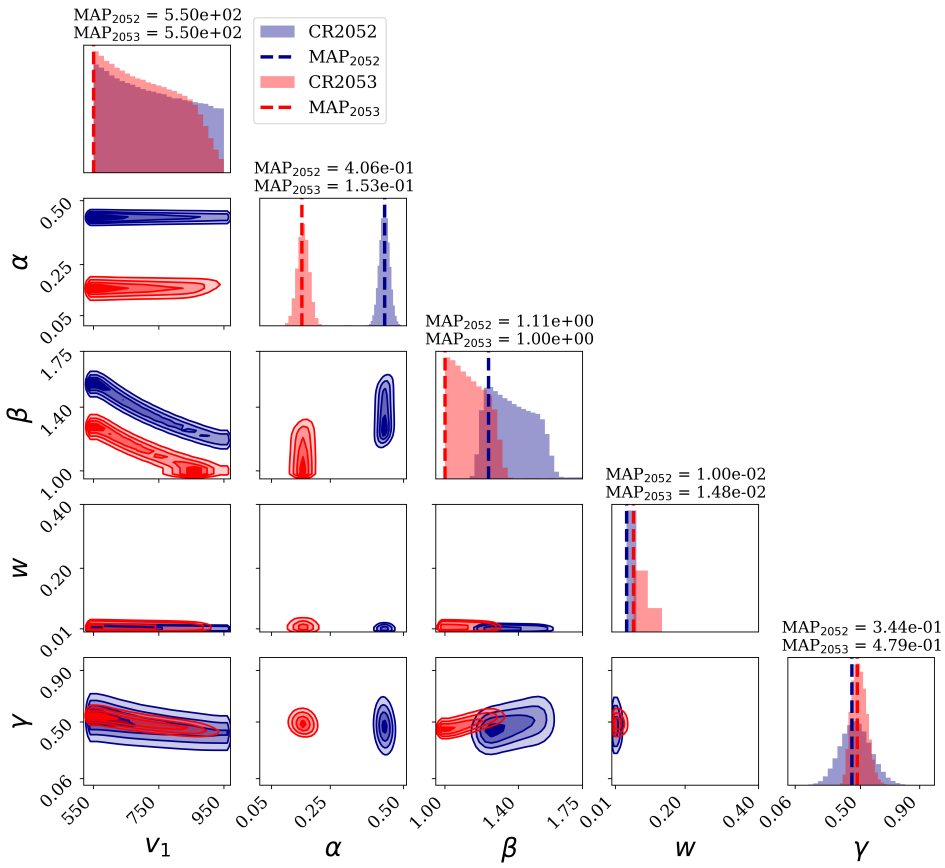

Figure 6. A corner plot of the posterior density of the five most influential parameters $v_1, \alpha, \beta, w, \gamma$ during CR 2052 (blue) and CR 2053 (red). The corner plot shows the MCMC samples in two-dimensional and one-dimensional projected parameter space. The dashed line shows the estimated MAP of each parameter.

and will also be able to successfully capture the parametric uncertainty on the predictions. The next subsection discusses our ensemble prediction numerical results.

4.3.2 Ensemble Prediction

We generate an ensemble prediction based on varying model parameters using MCMC posterior samples. The ensemble members are then used to compute ensemble statistics, such as the ensemble median and prediction interval. The *prediction interval* accounts for both the propagated parametric uncertainty and assumed model discrepancy errors (Smith, 2013, §9.4.3). The $(1-\alpha)\times 100\%$ prediction interval for a fixed but unknown new observation Z_i at time instance t_i is the interval $[Z_l, Z_u]$ such that

$$\mathbb{P}(Z_l \leq Z_i \leq Z_u) = 1 - \alpha,$$

where Z_i is independent of the data used to construct the random variables Z_l and Z_u (Smith, 2013, §9.4.1). We estimate the interval $[Z_l, Z_u]$ via computing the $\alpha/2$th and $1-\alpha/2$th quantiles of the set of ensemble members with added Gaussian model discrepancy errors. Figure 8(a) and Figure 9(a) show the median and 50% and 95% prediction interval of the 5×10^3 ensemble members during CR 2053 and CR 2052, respectively. The ensemble is generated using posterior samples trained separately on each CR. Figure 8(b) and Fig-

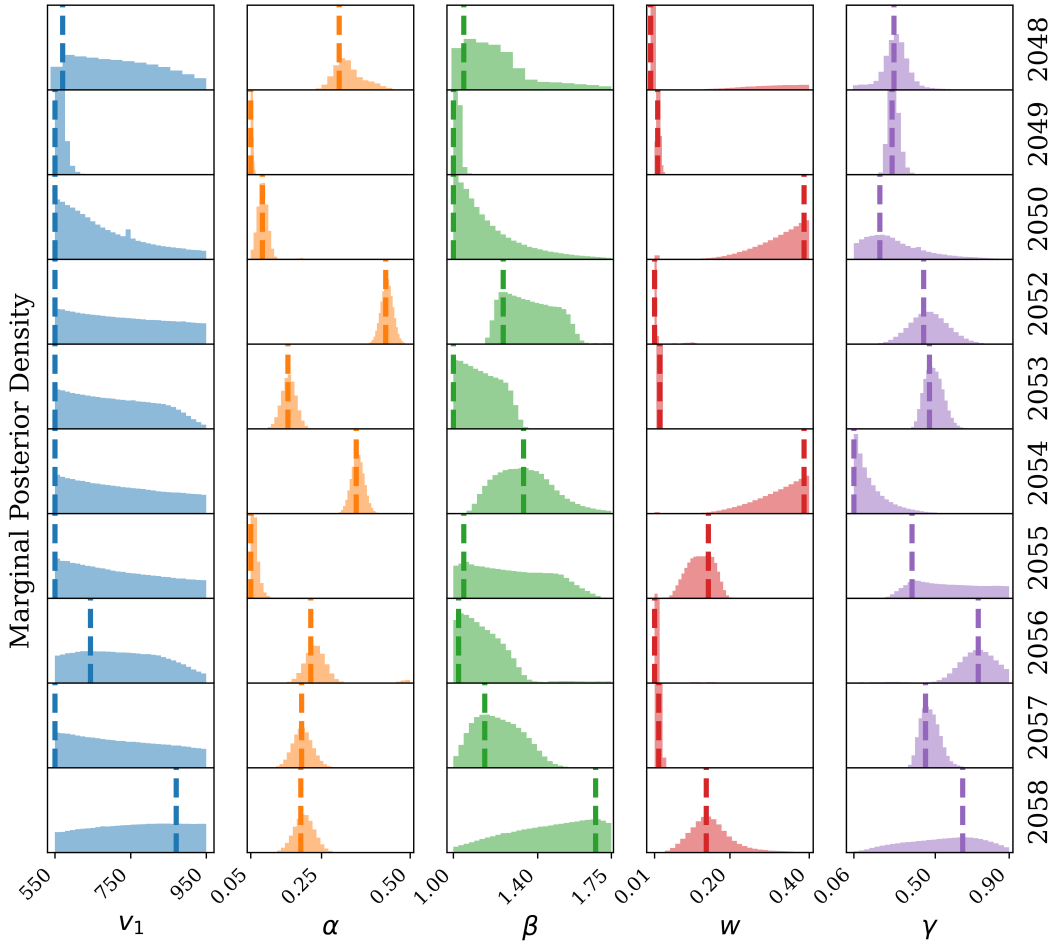

Figure 7. The marginal posterior densities of the five most influential parameters $v_1, \alpha, \beta, w, \gamma$ from CR 2048 to CR 2058 (excluding CR 2051). The dashed line shows the estimated MAP of each parameter. The marginal posteriors change substantially from one CR to the next.

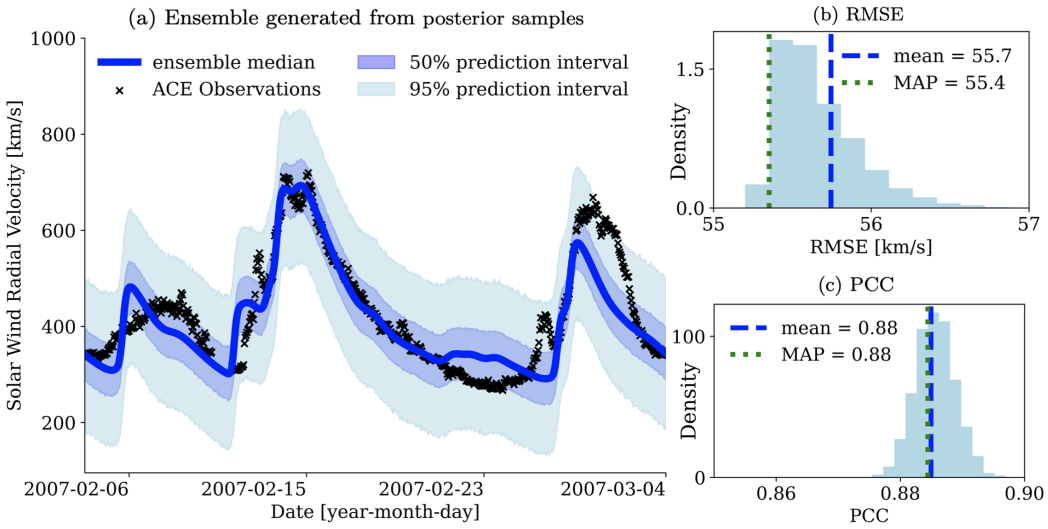

Figure 8. (a) Ensemble prediction with 5×10^3 ensemble members generated from posterior samples for CR 2053. The figure shows the ensemble statistics (median and prediction intervals) and ACE observations. Figures (b) and (c) show the RMSE and PCC of the ensemble in comparison to ACE observations, respectively.

ure 9(b) show a histogram of the RMSE of the ensemble members for each CR. Figure 8(c) and Figure 9(c) show a histogram of the PCC of the ensemble members for each CR. By comparing Figures 4(b/c) to Figures 8(b/c), it is apparent that the ensemble generated from the posterior density is able to substantially reduce the parametric uncertainty and improve the accuracy of the ensemble prediction. Specifically, the mean RMSE is reduced from $217.2\frac{\text{km}}{\text{s}}$ to $55.7\frac{\text{km}}{\text{s}}$, and the mean PCC is increased from 0.5 to 0.88. The results show that the proposed UQ framework is able to successfully reduce the uncertainty of the model parameters on the solar wind radial velocity prediction and should be utilized in further re-analysis studies.

5 Conclusions and Discussion

The PFSS→WSA→HUX model chain is commonly used to predict the ambient solar wind radial velocity near Earth. The model chain has eleven uncertain input parameters that can not be directly measured since they are mainly non-physical. We, therefore, propose a comprehensive UQ framework for quantifying and reducing the parametric uncertainty of the model chain. The proposed framework utilizes variance-based global sensitivity analysis to reduce the dimensionality of the parameter space, followed by Bayesian inference to learn the full parameter pdfs via MCMC. We apply the UQ framework on a time period spanning from CR 2048 to CR 2058 during the declining phase of solar cycle 23. The sensitivity analysis results show that $\beta, \gamma, \alpha, v_1, w$ are the five most influential parameters in the model chain. These parameters are all WSA parameters. We learned the posterior densities of the five most influential parameters using AIES (an MCMC sampler). The posterior samples are then used to generate an ensemble prediction and quantify the parametric uncertainty in the predicted solar wind velocity. We found that the ensemble results are able to accurately quantify the uncertainty in the predictions and thus suggest the proposed UQ framework should be utilized in further re-analysis studies employing the model chain.

The Bayesian inference numerical results also show that the posterior densities vary randomly from one CR to the next. This is mainly due to the following reasons: (1) the

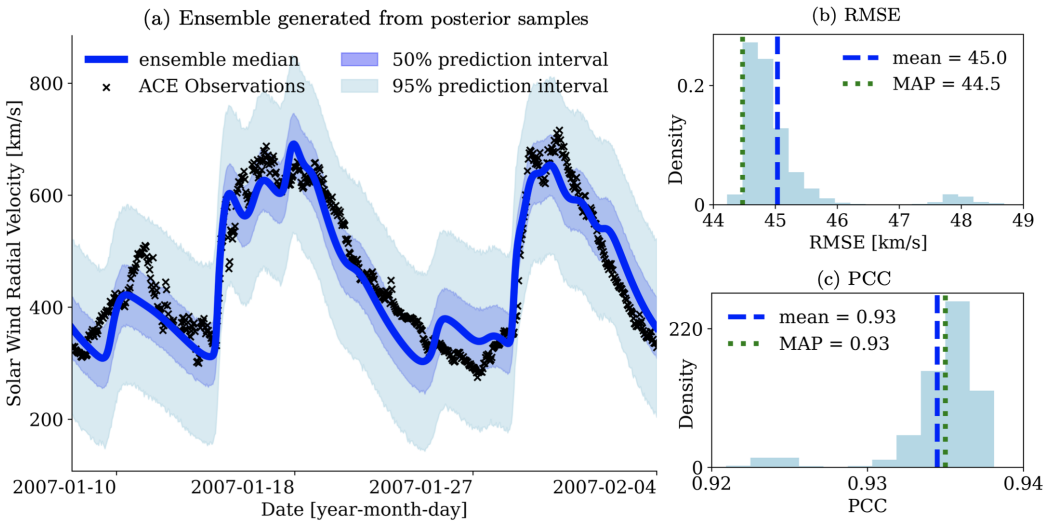

Figure 9. Same as Figure 8 for CR 2052.

model chain is not robust to the choice of WSA numerical parameters, and (2) the WSA model is overparameterized (i.e. needs to be reformulated for forecasting purposes). The reformulation of the WSA model will involve searching for a parsimonious model that is robust to its choice of parameters. Candidates of models that balance the trade-off between accuracy and parsimony can be found using sparse regression techniques with different regularization (Brunton et al., 2016). The optimal model can later be selected via the Bayesian or Akaike information criterion (Schwarz, 1978; Akaike, 1974). The substantial and unpredictable change in the posterior densities from one CR to the next questions the applicability of the model chain in operational real-time forecasting.

We suspect the drastic changes in the posterior densities are also due to the parameters trying to overcompensate the intrinsic and "hard-wired" limitations of each of the models (i.e. biases due to epistemic uncertainties). We next discuss such limitations. First, we do not have an accurate estimate of the photospheric fields (Poduval et al., 2020). There are differences between magnetograms from different observatories. There are also different saturation levels and noise (Riley et al., 2014). Second, the PFSS solutions rely on the existence of a spherical source surface, which does not exist (Riley et al., 2006). The sensitivity analysis results show that the choice of the source surface height is non-influential on the predicted solar wind velocity at L1, yet in the analysis we assume it exists. Also, the fields are not potential, particularly around active regions. Third, the WSA model has known inaccuracies, e.g. the expansion factor in the vicinity of pseudostreamers (Riley et al., 2015), as well as unknown inaccuracies. Fourth, the HUX model assumes only radial propagation and neglects external forces and the pressure gradient (Riley & Lionello, 2011). Fifth, time dependence is not included in synoptic maps and all throughout the model chain. Thus, the physics simplifications in the model chain introduce model discrepancies between the spacecraft observations and model predictions. We assume such discrepancies are Gaussian distributed in the Bayesian inference setup. This is generally a reasonable assumption, which is necessary in order to formulate the likelihood in the Bayesian setting, yet it is important to point out that the model chain discrepancies are structured and are not i.i.d.

Future studies can incorporate the proposed UQ framework for learning the posterior densities of uncertain parameters for various (and more complex) space weather models, for example, the WSA-Enlil model (Parsons et al., 2011). It will be interesting to ap-

Table A1. The analytically computed Sobol' sensitivity indices of the WS model for $f_p = 10, 10^2, 10^4$. The results show that α is the most influential parameter (in comparison to v_0 and v_1). Additionally, the indices indicate that v_0 is more influential when f_p is high and that v_1 is more influential when f_p is low.

f_p	S_{v_0}	S_{v_1}	S_α	S_{v_0,v_1}	$S_{v_0,\alpha}$	$S_{v_1,\alpha}$	T_{v_0}	T_{v_1}	T_α
10	0.061	0.383	0.512	0	0.008	0.034	0.07	0.417	0.554
10^2	0.131	0.133	0.679	0	0.011	0.045	0.143	0.178	0.735
10^4	0.289	0.036	0.623	0	0.01	0.041	0.3	0.077	0.674

ply the proposed UQ framework to WSA-Enlil to make sure the WSA posteriors do not change drastically in time and verify that the WSA-Enlil model is reliable for real-time forecasting. Depending on the computational resources and computational complexity of the model at hand, one might need to incorporate surrogate models (computationally efficient approximate models), such as projection-based reduced-order models (Benner et al., 2015; Issan & Kramer, 2022) and interpolatory surrogates (Xiu & Karniadakis, 2002), to compute Sobol' sensitivity indices and run MCMC. If the model is computationally efficient (i.e. order of seconds/minutes) we recommend using the MC methods presented in this study as they are unbiased estimators. Other unbiased estimators include multi-fidelity estimators, see Peherstorfer et al. (2018) for a detailed survey.

Appendix A Global Sensitivity Analysis of the Wang-Sheeley Model: Analytic Results

The Wang-Sheeley (WS) semi-empirical model developed by Wang and Sheeley (1990) is based on the inverse relationship between the solar wind speed and the magnetic field expansion factor f_p (defined in Eq. (2)). The WS model relation is given by

$$v_{\text{ws}}(f_p, v_0, v_1, \alpha) = v_0 + \frac{v_1 - v_0}{f_p^\alpha}$$

where v_0 and v_1 correspond to the minimum and maximum solar wind velocities, f_p is the magnetic field expansion factor, and α is an additional numerical parameter.

The Sobol' sensitivity indices described in Eqns. (5)–(6) for the WS model parameters v_0, v_1, α can be computed analytically (symbolically) if we assume the model parameters are independent and have uniform priors. In contrast, for the PFSS, WSA, and HUX models, the sensitivity indices can only be approximated numerically via MC integration, see Section 3.3. We set the priors to be uniform with ranges listed in Table 1. Table A1 shows the Sobol' sensitivity indices of the three model parameters v_0, v_1, α for $f_p = 10, 10^2, 10^4$. Larger f_p corresponds to slower solar wind velocity, in which case v_0 becomes more influential, and v_1 becomes less influential. The second-order indices show that v_0 and v_1 do not interact and that α's interaction with v_0 and v_1 is minor compared to the first-order indices. By the first- and total-order indices of α, we can conclude that it is the most influential parameter independent of f_p (in comparison to v_0 and v_1) which agrees with the ordering in the WSA model, see Section 3.4.

Acronyms

UQ Uncertainty Quantification
QoI Quantity of Interest
MAP Maximum a posteriori

MCMC Markov chain Monte Carlo
PFSS Potential-field Source-surface
WSA Wang-Sheeley-Arge
HUX Heliospheric Upwind eXtrapolation
GONG Global Oscillations Network Group
ACE Advanced Composition Explorer
RMSE Root mean squared error
CR Carrington rotation
AIES Affine Invariant Ensemble Sampler
MC Monte Carlo
pdf probability density function

Open Research

The public repository `https://github.com/opaliss/Parameter_Estimation_Solar_Wind` contains a collection of Jupyter notebooks in Python 3.9 containing the code and data used in this study. The GONG synoptic maps are retrieved from `https://gong.nso.edu/data/magmap/crmap.html` and the ACE spacecraft observations can be found at `https://cdaweb.gsfc.nasa.gov/index.html/`.

Acknowledgments

O.I. and B.K. were partially supported by the National Science Foundation under Award 2028125 for "SWQU: Composable Next Generation Software Framework for Space Weather Data Assimilation and Uncertainty Quantification". E.C. was partially supported by NASA grants 80NSSC20K1580 "Ensemble Learning for Accurate and Reliable Uncertainty Quantification" and 80NSSC20K1275 "Global Evolution and Local Dynamics of the Kinetic Solar Wind". P.R. acknowledges support from NASA (80NSSC18K0100, NNX16AG86G, 80NSSC18K1129, 80NSSC18K0101, 80NSSC20K1285, 80NSSC18K1201, and NNN06AA01C), NOAA (NA18NWS4680081), and the U.S. Air Force (FA9550-15-C-0001).

References

Akaike, H. (1974). A new look at the statistical model identification. *IEEE Transactions on Automatic Control*, *19*(6), 716-723. doi: 10.1109/TAC.1974.1100705

Altschuler, M. D., & Newkirk, G. (1969, September). Magnetic Fields and the Structure of the Solar Corona. I: Methods of Calculating Coronal Fields. *Solar Physics*, *9*(1), 131-149. doi: 10.1007/BF00145734

Arden, W. M., Norton, A. A., & Sun, X. (2014, March). A "breathing" source surface for cycles 23 and 24. *Journal of Geophysical Research (Space Physics)*, *119*(3), 1476-1485. doi: 10.1002/2013JA019464

Arge, C., Luhmann, J., Odstrcil, D., Schrijver, C., & Li, Y. (2004). Stream structure and coronal sources of the solar wind during the May 12th, 1997 CME. *Journal of Atmospheric and Solar-Terrestrial Physics*, *66*(15), 1295-1309. doi: https://doi.org/10.1016/j.jastp.2004.03.018

Bailey, R. L., Reiss, M. A., Arge, C. N., Möstl, C., Henney, C. J., Owens, M. J., ... Hinterreiter, J. (2021). Using Gradient Boosting Regression to Improve Ambient Solar Wind Model Predictions. *Space Weather*, *19*(5), e2020SW002673. doi: https://doi.org/10.1029/2020SW002673

Benner, P., Gugercin, S., & Willcox, K. (2015). A Survey of Projection-Based Model Reduction Methods for Parametric Dynamical Systems. *SIAM Review*, *57*(4), 483-531. doi: 10.1137/130932715

Brunton, S. L., Proctor, J. L., & Kutz, J. N. (2016, March). Discovering governing equations from data by sparse identification of nonlinear dynamical systems. *Proceedings of the*

National Academy of Sciences, *113*(15), 3932-3937. doi: 10.1073/pnas.1517384113

Caplan, R. M., Downs, C., Linker, J. A., & Mikić, Z. (2021, July). Variations in finite-difference potential fields. *The Astrophysical Journal*, *915*(1), 44. doi: 10.3847/1538-4357/abfd2f

Foreman-Mackey, D., Hogg, D. W., Lang, D., & Goodman, J. (2013, March). emcee: The MCMC Hammer. *Publications of the Astronomical Society of the Pacific*, *125*(925), 306. doi: 10.1086/670067

Goodman, J., & Weare, J. (2010, Jan). Ensemble samplers with affine invariance. *Communications in Applied Mathematics and Computational Science*, *5*(1), 65-80. doi: 10.2140/camcos.2010.5.65

Halton, J. H. (1960, December). On the Efficiency of Certain Quasi-Random Sequences of Points in Evaluating Multi-Dimensional Integrals. *Numer. Math.*, *2*(1), 84–90. doi: 10.1007/BF01386213

Harvey, J. W., Hill, F., Hubbard, R. P., Kennedy, J. R., Leibacher, J. W., Pintar, J. A., ... Yasukawa, E. (1996). The Global Oscillation Network Group (GONG) Project. *Science*, *272*(5266), 1284-1286. doi: 10.1126/science.272.5266.1284

Hastings, W. K. (1970, 04). Monte Carlo sampling methods using Markov chains and their applications. *Biometrika*, *57*(1), 97-109. doi: 10.1093/biomet/57.1.97

Hill, F. (2018). The Global Oscillation Network Group Facility—An Example of Research to Operations in Space Weather. *Space Weather*, *16*(10), 1488-1497. doi: https://doi.org/10.1029/2018SW002001

Issan, O., & Kramer, B. (2022). Predicting Solar Wind Streams from the Inner-Heliosphere to Earth via Shifted Operator Inference. *Journal of Computational Physics*, *3473*, 111689.

Issan, O., & Riley, P. (2022). Theoretical Refinements to the Heliospheric Upwind eXtrapolation Technique and Application to in-situ Measurements. *Frontiers in Astronomy and Space Sciences*, *8*, 245. doi: 10.3389/fspas.2021.795323

Janon, A., Klein, T., Lagnoux, A., Nodet, M., & Prieur, C. (2014). Asymptotic normality and efficiency of two Sobol index estimators. *ESAIM: Probability and Statistics*, *18*, 342–364.

Jansen, M. J. (1999). Analysis of variance designs for model output. *Computer Physics Communications*, *117*(1), 35-43.

Jivani, A., Sachdeva, N., Huang, Z., Chen, Y., van der Holst, B., Manchester, W., ... Toth, G. (2022). Global Sensitivity Analysis and Uncertainty Quantification for Background Solar Wind Using the Alfvén Wave Solar Atmosphere Model. *Space Weather*, *21*(1), e2022SW003262. doi: https://doi.org/10.1029/2022SW003262

Kruse, A., Heidrich-Meisner, V., Wimmer-Schweingruber, R., & Hauptmann, M. (2020, May). An elliptic expansion of the potential field source surface model. *Astronomy & Astrophysics*, *638*. doi: 10.1051/0004-6361/202037734

Kumar, S., & Srivastava, N. (2022). A Parametric Study of Performance of Two Solar Wind Velocity Forecasting Models During 2006–2011. *Space Weather*, *20*(9), e2022SW003069. doi: https://doi.org/10.1029/2022SW003069

Lee, C. O., Luhmann, J. G., Hoeksema, J. T., Sun, X., Arge, C. N., & de Pater, I. (2011, April). Coronal Field Opens at Lower Height During the Solar Cycles 22 and 23 Minimum Periods: IMF Comparison Suggests the Source Surface Should Be Lowered. *Solar Physics*, *269*(2), 367-388. doi: 10.1007/s11207-010-9699-9

Linker, J. A., Mikić, Z., Biesecker, D. A., Forsyth, R. J., Gibson, S. E., Lazarus, A. J., ... Thompson, B. J. (1999, May). Magnetohydrodynamic modeling of the solar corona during Whole Sun Month. *Journal of Geophysical Research*, *104*(A5), 9809-9830. doi: 10.1029/1998JA900159

Liu, X., Feng, X., Lv, J., Wang, X., & Zhang, M. (2022). Direct discontinuous Galerkin method for potential magnetic field solutions. *Frontiers in Astronomy and Space Sciences*, *9*. doi: 10.3389/fspas.2022.1055969

McComas, D. J., Bame, S. J., Barker, P., Feldman, W. C., Phillips, J. L., Riley, P., & Griffee, J. W. (1998, July). Solar Wind Electron Proton Alpha Monitor (SWEPAM)

for the Advanced Composition Explorer. *Space Science Reviews*, *86*, 563-612. doi: 10.1023/A:1005040232597

McKay, M., Beckman, R., & Conover, W. (1979, 05). A comparison of three methods for selecting values of input variables in the analysis of output from a computer code. *Technometrics*, *21*, 239-245. doi: 10.1080/00401706.1979.10489755

Meadors, G. D., Jones, S. I., Hickmann, K. S., Arge, C. N., Godinez-Vasquez, H. C., & Henney, C. J. (2020). Data Assimilative Optimization of WSA Source Surface and Interface Radii using Particle Filtering. *Space Weather*, *18*(5), e2020SW002464. doi: https://doi.org/10.1029/2020SW002464

Metropolis, N., Rosenbluth, A. W., Rosenbluth, M. N., Teller, A. H., & Teller, E. (1953, June). Equation of State Calculations by Fast Computing Machines. *Journal of Chemical Physics*, *21*(6), 1087-1092. doi: 10.1063/1.1699114

Mikić, Z., Downs, C., Linker, J. A., Caplan, R. M., Mackay, D. H., Upton, L. A., ... others (2018). Predicting the corona for the 21 August 2017 total solar eclipse. *Nature Astronomy*, 1.

Milton, J., & Arnold, J. (2003). *Introduction to Probability and Statistics: Principles and Applications for Engineering and the Computing Sciences*. McGraw-Hill.

Moldwin, M. (2008). *An introduction to space weather*. Cambridge University Press. doi: 10.1017/CBO9780511801365

Monod, H., Naud, C., & Makowski, D. (2006, 01). Uncertainty and sensitivity analysis for crop models. *Working with Dynamic Crop Models*, 55-100.

Morris, M. D. (1991). Factorial Sampling Plans for Preliminary Computational Experiments. *Technometrics*, *33*(2), 161-174.

Nikolić, L. (2019). On Solutions of the PFSS Model With GONG Synoptic Maps for 2006–2018. *Space Weather*, *17*(8), 1293-1311. doi: https://doi.org/10.1029/2019SW002205

Odstrcil, D., & Pizzo, V. J. (1999). Distortion of the interplanetary magnetic field by three-dimensional propagation of coronal mass ejections in a structured solar wind. *Journal of Geophysical Research: Space Physics*, *104*(A12), 28225-28239. doi: https://doi.org/10.1029/1999JA900319

Parsons, A., Biesecker, D., Odstrcil, D., Millward, G., Hill, S., & Pizzo, V. (2011). Wang-Sheeley-Arge–Enlil Cone Model Transitions to Operations. *Space Weather*, *9*(3). doi: https://doi.org/10.1029/2011SW000663

Peherstorfer, B., Willcox, K., & Gunzburger, M. (2018). Survey of Multifidelity Methods in Uncertainty Propagation, Inference, and Optimization. *SIAM Review*, *60*(3), 550-591. doi: 10.1137/16M1082469

Poduval, B., Petrie, G., & Bertello, L. (2020). Uncertainty estimates of solar wind prediction using HMI photospheric vector and spatial standard deviation synoptic maps. *Solar Physics*, *295*, 1-20.

Puy, A., Becker, W., Lo Piano, S., & Saltelli, A. (2022, April 30). A comprehensive comparison of total-order estimators for global sensitivity analysis. *International Journal for Uncertainty Quantification*, *12*(2), 1-18.

Reiss, M. A., MacNeice, P. J., Mays, L. M., Arge, C. N., Möstl, C., Nikolić, L., & Amerstorfer, T. (2019, Feb). Forecasting the Ambient Solar Wind with Numerical Models. I. On the Implementation of an Operational Framework. *The Astrophysical Journal*, *240*(2), 35. doi: 10.3847/1538-4365/aaf8b3

Reiss, M. A., MacNeice, P. J., Muglach, K., Arge, C. N., Möstl, C., Riley, P., ... Amerstorfer, U. (2020, March). Forecasting the Ambient Solar Wind with Numerical Models. II. An Adaptive Prediction System for Specifying Solar Wind Speed near the Sun. *The Astrophysical Journal*, *891*(2), 165. doi: 10.3847/1538-4357/ab78a0

Reiss, M. A., Muglach, K., Mullinix, R., Kuznetsova, M. M., Wiegand, C., Temmer, M., ... Samara, E. (2022). Unifying the validation of ambient solar wind models. *Advances in Space Research*. doi: https://doi.org/10.1016/j.asr.2022.05.026

Richardson, I., Cliver, E., & Cane, H. (2000). Sources of geomagnetic activity over the solar cycle: Relative importance of coronal mass ejections, high-speed streams, and slow

solar wind. *Journal of Geophysical Research: Space Physics*, *105*(A8), 18203-18213.
Riley, P., Ben-Nun, M., Linker, J., Mikić, Z., Svalgaard, L., Harvey, J., ... Ulrich, R. (2014). A multi-observatory inter-comparison of line-of-sight synoptic solar magnetograms. *Solar Physics*, *289*(3), 769-792.
Riley, P., Downs, C., Linker, J. A., Mikić, Z., Lionello, R., & Caplan, R. M. (2019, March). Predicting the Structure of the Solar Corona and Inner Heliosphere during Parker Solar Probe's First Perihelion Pass. *The Astrophysical Journal*, *874*(2), L15. doi: 10.3847/2041-8213/ab0ec3
Riley, P., & Issan, O. (2021). Using a Heliospheric Upwinding eXtrapolation Technique to Magnetically Connect Different Regions of the Heliosphere. *Frontiers in Physics*, *9*, 268. doi: 10.3389/fphy.2021.679497
Riley, P., Linker, J. A., & Arge, C. N. (2015). On the role played by magnetic expansion factor in the prediction of solar wind speed. *Space Weather*, *13*(3), 154-169. doi: https://doi.org/10.1002/2014SW001144
Riley, P., Linker, J. A., Lionello, R., & Mikić, Z. (2012). Corotating interaction regions during the recent solar minimum: The power and limitations of global MHD modeling. *Journal of Atmospheric and Solar-Terrestrial Physics*, *83*, 1-10. (Corotating Interaction Regions from Sun to Earth: Modeling their formation, evolution and geoeffectiveness) doi: https://doi.org/10.1016/j.jastp.2011.12.013
Riley, P., Linker, J. A., & Mikić, Z. (2001). An empirically-driven global MHD model of the solar corona and inner heliosphere. *Journal of Geophysical Research: Space Physics*, *106*(A8), 15889-15901. doi: https://doi.org/10.1029/2000JA000121
Riley, P., Linker, J. A., Mikić, Z., Lionello, R., Ledvina, S. A., & Luhmann, J. G. (2006, Dec). A Comparison between Global Solar Magnetohydrodynamic and Potential Field Source Surface Model Results. *The Astrophysical Journal*, *653*(2), 1510. doi: 10.1086/508565
Riley, P., & Lionello, R. (2011, June). Mapping Solar Wind Streams from the Sun to 1 AU: A Comparison of Techniques. *Solar Physics*, *270*, 575-592. doi: 10.1007/s11207-011-9766-x
Roberts, G. O., & Rosenthal, J. S. (2004). General state space Markov chains and MCMC algorithms. *Probability Surveys*, *1*, 20-71. doi: 10.1214/154957804100000024
Saltelli, A. (2002). Making best use of model evaluations to compute sensitivity indices. *Computer Physics Communications*, *145*(2), 280-297. doi: https://doi.org/10.1016/S0010-4655(02)00280-1
Saltelli, A., Ratto, M., Andres, T., Campolongo, F., Cariboni, J., Gatelli, D., ... Tarantola, S. (2008). *Global sensitivity analysis. the primer* (Vol. 304).
Schatten, K. H., Wilcox, J. M., & Ness, N. F. (1969, March). A model of interplanetary and coronal magnetic fields. *Solar Physics*, *6*(3), 442-455. doi: 10.1007/BF00146478
Schwarz, G. (1978). Estimating the Dimension of a Model. *The Annals of Statistics*, *6*(2), 461-464. doi: 10.1214/aos/1176344136
Smith, R. C. (2013). *Uncertainty Quantification: Theory, Implementation, and Applications*. Society for Industrial and Applied Mathematics.
Sobol', I. (1967). On the distribution of points in a cube and the approximate evaluation of integrals. *USSR Computational Mathematics and Mathematical Physics*, *7*(4), 86-112. doi: https://doi.org/10.1016/0041-5553(67)90144-9
Sobol', I. (2001). Global sensitivity indices for nonlinear mathematical models and their Monte Carlo estimates. *Mathematics and Computers in Simulation*, *55*(1), 271-280. doi: https://doi.org/10.1016/S0378-4754(00)00270-6
Stansby, D., Rai, Y., Argall, M., Broll, J., Haythornthwaite, R., Erwin, N., ... et al. (2021, March). *heliopython/heliopy: Heliopy 0.15.3.* Zenodo. doi: 10.5281/zenodo.4643882
Stansby, D., Yeates, A., & Badman, S. T. (2020). pfsspy: A python package for potential field source surface modelling. *Journal of Open Source Software*, *5*(54), 2732. doi: 10.21105/joss.02732
Toth, G., Sokolov, I. V., Gombosi, T. I., Chesney, D. R., Clauer, C. R., De Zeeuw, D. L., ... Kóta, J. (2005). Space weather modeling framework: A new tool for the space

science community. *Journal of Geophysical Research: Space Physics*, *110*(A12). doi: https://doi.org/10.1029/2005JA011126

van der Holst, B., Sokolov, I. V., Meng, X., Jin, M., W. B. Manchester, I., Tóth, G., & Gombosi, T. I. (2014, Jan). Alfvén Wave Solar Model (AWSoM): Coronal Heating. *The Astrophysical Journal*, *782*(2), 81. doi: 10.1088/0004-637x/782/2/81

Wang, Y. M., & Sheeley, J., N. R. (1990, June). Solar Wind Speed and Coronal Flux-Tube Expansion. *The Astrophysical Journal*, *355*, 726. doi: 10.1086/168805

Wang, Y. M., & Sheeley, J., N. R. (1995, July). Solar Implications of Ulysses Interplanetary Field Measurements. *Astrophysical Journal*, *447*, 143. doi: 10.1086/309578

Xiu, D., & Karniadakis, G. E. (2002). The Wiener–Askey Polynomial Chaos for Stochastic Differential Equations. *SIAM Journal on Scientific Computing*, *24*(2), 619-644. doi: 10.1137/S1064827501387826